ADVANCED FUNCTIONAL MATERIALS
www.afm-journal.de

Hydrogel-Based Self-Powered, Oxygen-Resistant, and Flexible Sensors for Ultrasensitive and Selective NO_2 Detection

*Qiongling Ding, Yibing Luo, Wenxiong Shi, Hao Wang, Jianye Li, Yubin Zhou, Xiaobo Zhu, Dijie Yao, Zixuan Wu, Kai Tao, Fei Liu, Pengcheng Xu, Hu Long, Pengbo Wan, Fengwei Huo, and Jin Wu**

Flexible nitrogen dioxide (NO_2) sensors hold great promise for timely protection of both the environment and human health. However, current NO_2 sensing technologies face the dilemma of substantial power consumption, susceptibility to oxygen interference, and insufficient wearing comfort, seriously hindering their practical applications. Herein, a self-powered, oxygen-resistant, and flexible NO_2 sensor with a cell structure is proposed based on dense polyacrylamide-calcium alginate hydrogel network and a heterogeneous metal electrode pair with similar electrode potentials. The resulting NO_2 sensor exhibits an ultrahigh sensitivity of 307.17% per ppm, an ultra-low detection limit of 2.86 ppb, and high selectivity relative to the strongest interfering gas (oxygen), originating from the tiny electromotive force provided by this self-powered sensor exclusively driving the reduction of NO_2. The superior NO_2 sensing performance of the sensor is synergistically attributed to the catalysis of the NO_2 reduction reaction by the employed Ag electrodes and the inhibition of NO_2 solubilization by the dense hydrogel networks. The incorporation of glycerol into the hydrogel further enhances the environmental tolerance and stability of the device. Thanks to these, remote and real-time alarms for trace NO_2 leaks are implemented in both aerobic and anaerobic environments by connecting the developed sensor to a self-designed wireless sensing system.

1. Introduction

With the rapid development of Internet of Things (IoT) technology, flexible gas sensors have received extensive attention due to their potential application prospects in diverse environmental protection, smart healthcare, safety, artificial intelligence, and soft robotics.[1–4] Typically, nitrogen dioxide (NO_2) is one of the common atmospheric pollutants originating from vehicle exhaust, industrial emissions, and fuel combustion, which seriously threatens human health and the living environment.[5,6] Given that, the development of flexible NO_2 sensors that can be integrated into wearable devices is highly desirable amid the increasing global air pollution, enabling real-time NO_2 monitoring and timely hazard prediction, which puts forward higher requirements for their sensing performance, operating temperature and safety, power consumption, and wearing comfort. Among

Q. Ding, Y. Luo, H. Wang, J. Li, D. Yao, F. Liu, J. Wu
State Key Laboratory of Optoelectronic Materials and Technologies and the Guangdong Province Key Laboratory of Display Material and Technology
School of Electronics and Information Technology
Sun Yat-sen University
Guangzhou 510275, China
E-mail: wujin8@mail.sysu.edu.cn

X. Zhu
State Key Laboratory of Advanced Marine Materials, Ningbo Institute of Materials Technology and Engineering
Chinese Academy of Sciences
Ningbo 315201, China

Q. Ding, P. Xu, J. Wu
State Key Laboratory of Transducer Technology
Shanghai 200050, P. R. China

W. Shi
Institute for New Energy Materials and Low Carbon Technologies
School of Materials Science and Engineering
Tianjin University of Technology
Tianjin 300384, China

Y. Zhou
Dongguan Key Laboratory of Advanced Drug Delivery and Biosensing Research and Development
School of Pharmacy and Dongguan Innovation Institute
Guangdong Medical University
Dongguan 523808, China

Q. Ding, H. Long
State Key Laboratory of Intelligent Manufacturing Equipment and Technology
Wuhan 430074, China

Z. Wu
Research Center of Flexible Sensing Materials and Devices
School of Applied Physics and Materials
Wuyi University
Jiangmen 529020, China

The ORCID identification number(s) for the author(s) of this article can be found under https://doi.org/10.1002/adfm.202512817

DOI: 10.1002/adfm.202512817

previously reported gas sensors, electrochemical devices simultaneously feature the advantages of low cost and the ability to operate at room or even sub-zero temperatures, and can avoid the potential thermal safety hazards and high power consumption associated with the high operating temperatures of traditional well-researched metal oxide-based chemiresistive gas sensors.[7,8] Instead of the change in bulk phase resistance induced by gas adsorption, the response of electrochemical gas sensors stems from the increase in current/potential following oxidation/reduction of the target gas at the electrode-electrolyte (electron-ion) interface.[9] Thereby, the gas sensing performance of such devices can be optimized mainly by interfacial modification, without the need for more complex and sophisticated strategies to achieve a breakthrough in the increase of the specific surface area of functional materials.

Nevertheless, the liquid electrolytes used in conventional electrochemical gas sensors are susceptible to volatilization and leakage, resulting in device failures and potential hazards to humans or the environment.[10] Furthermore, traditional electrochemical sensors are rigid, limiting their application in wearable electronic devices. Hydrogels, composed of polymer networks dispersed in water, exhibit remarkable stretchability, ionic transport characteristics, biocompatibility, multi-stimulus responsiveness, and chemical designability.[11–15] Therefore, hydrogels can be exploited as an ideal candidate to serve as solid-state electrolytes to construct flexible electrochemical sensors that can withstand various deformations and prevent the evaporation of traditional liquid electrolytes. For example, Wu et al. have proposed a highly stretchable electrochemical NO_2 sensor based on polyacrylamide-carrageenan (PAM-Carr) hydrogel, with a high sensitivity of 119.9% per ppm.[16] However, the NO_2 sensing performance of reported electrochemical sensors is greatly degraded in the atmosphere with oxygen, greatly limiting their application scenarios. This can be attributed to the fact that low-concentration NO_2 has difficulty in competing with the large amount of oxygen molecules in the ambient environment for undergoing reduction reactions at the electrode interface, giving rise to severe interference of oxygen on NO_2 sensing. Even for oxide-based chemiresistive devices, their sensing performance relies heavily on the pre-adsorption of oxygen and is thus severely affected by oxygen level.[17,18] So far, portable NO_2 sensors that are resistant to oxygen interference or independent of oxygen have rarely been reported, but further development is urgently needed as oxygen is ubiquitous and variable in a variety of application scenarios.

In addition, most current gas sensors need to be equipped with external batteries or energy storage devices for power supply, resulting in poor wearing comfort and sustainability, large size, and high cost. Although flexible batteries have made a lot of progress in recent years, their output performance is not ideal compared with traditional rigid ones, limiting their application in wearable devices.[19–21] To address this, some strategies are proposed to construct all-in-one self-powered sensing systems that do not require continuous drive from an external power source by coupling the sensors with energy harvesting devices (piezoelectric, triboelectric, and thermoelectric generators), so that the devices can obtain energy from the surrounding environment for sustained operation,[22–25] minimizing power consumption and promoting carbon neutralization and portability. However, the operation of such devices always requires a stable and continuous supply of external energy, such as mechanical vibration, heat, wind, etc.[26–28] Otherwise, they struggle to maintain a constant output, and their sensing function is susceptible to interference. Although sustainable and consistent electrical output can be realized with synergistic and complementary hybrid generators, this approach unfortunately leads to an increase in the complexity and size of sensing systems.[29,30] In comparison, a primary battery can spontaneously convert chemical energy into electrical energy in a static manner and provides a stable output.[31,32] Inspired by this, it is highly anticipated to develop a flexible and self-powered all-in-one gas sensor with a galvanic cell structure based on hydrogel electrolyte, enabling long-term stable and anti-interference monitoring as wearable electronics.

Herein, considering that NO_2, which has free radical properties, potentially be more easily reduced on the electrode compared to oxygen, we propose a novel strategy to construct a self-powered, oxygen-resistant and flexible cell-structured NO_2 sensor by applying a metal electrode pair (Cu and Ag) with similar electrode potentials onto a tough and dense PAM-calcium alginate (CA) hydrogel electrolyte. As a result, NO_2 can be selectively reduced to produce a Faraday current driven by the tiny electromotive force (EMF) provided by this prepared sensor, but oxygen cannot, thereby enabling NO_2 sensing without oxygen interference. The sensor exhibits ultra-high sensitivity (307.17%/ppm), exceptional selectivity, ultra-low LOD (2.86 ppb), and similar NO_2 sensing performance in different oxygen concentrations (0%, 20%, and 60% O_2). By introducing organic solvents into the PAM-CA hydrogel, the stability of hydrogel and device is greatly improved, with similar responsiveness under different humidity and temperatures. Reasonable analyses reveal that the responsiveness of the sensor is closely related to the electrode type and hydrogel components. On the one hand, the working electrode (Ag) in the sensor plays an important role in catalyzing the NO_2 reduction. On the other hand, the applied PAM-CA hydrogel, featuring a dense double network structure, has the capacity to modulate the NO_2 reaction path, so that more NO_2 molecules adsorbed at the hydrogel-electrode interface can participate in electrode reactions that can cause large current changes and lead to an increase in device sensitivity. After combining with circuitry and wireless transmission technology, the developed device is then applied to the recognition and alarm of trace NO_2 leakage

K. Tao
The Ministry of Education Key Laboratory of Micro and Nano Systems for Aerospace
School of Mechanical Engineering
Northwestern Polytechnical University
Xi'an 710072, P. R. China

P. Wan
College of Materials Science and Engineering
State Key Laboratory of Organic-Inorganic Composites
Beijing University of Chemical Technology
Beijing 100029, China

F. Huo
State Key Laboratory of Flexible Electronics (LoFE) & Institute of Advanced Materials (IAM)
School of Flexible Electronics (Future Technologies)
Nanjing Tech University (Nanjing Tech)
Nanjing 211816, China

in different scenarios, including aerobic and anaerobic environments, demonstrating its feasibility in practical applications.

2. Results and Discussion

2.1. Design of Self-Powered, Oxygen-Resistant, and Flexible NO_2 Sensor

In conventional electrochemical self-powered NO_2 sensors, both oxygen and NO_2 can be readily reduced at the cathode driven by their large EMF to generate Faraday currents due to their strong oxidizing nature, leading to the problem of device susceptibility to oxygen (**Figure 1a**). Since NO_2 is capable of direct radical reactions, it is kinetically highly oxidizing.[33] In contrast, for the oxygen reduction reaction (ORR), the O-O bond in the oxygen molecule needs to be broken first and multiple electron transfer processes are involved, thus the reduction of oxygen may need to be driven by a higher EMF compared to NO_2. Inspired by this, an electrochemical self-powered and oxygen-resistant NO_2 sensor is expected to be realized by providing a tiny EMF, capable of driving only the reduction of NO_2 and struggling to drive the ORR to occur. However, the realization of this concept in self-powered electrochemical devices assembled from conventional highly conductive liquid electrolytes is challenging due to the more pronounced difference in electrode potential between two metal electrodes upon contact with the electrolyte and the corresponding difficulty in providing the required minimal EMF. To address this, we propose to utilize hydrogel materials with lower conductivity as electrolyte to construct cell-structured self-powered NO_2 sensors by applying two heterogeneous metal electrodes with similar potentials on the two ends of hydrogel, which not only further reduces the EMF of the device, but also endows it with excellent flexibility and stretchability. In this way, self-powered, oxygen-interference-free, and flexible NO_2 sensors can be constructed, which can play an important role in the field of wearable devices.

In recent years, PAM-based hydrogels manifest obvious advantages in the construction of wearable electronic devices due to their superior flexibility, cost-effectiveness, good chemical stability, simple, and scalable production.[34–36] In order to adapt to applications in different fields, we have explored incorporating another heterogeneous CA polymer network into the PAM hydrogel to further enhance its network density, mechanical strength, and toughness. The fabrication process of the PAM-CA double-network hydrogel is illustrated in Figure 1b, with the details presented in the Experimental section. In the first stage, PAM-sodium alginate (SA) hydrogel is prepared through a one-pot sol-gel polymerization process, in which acrylamide (AM) monomer molecules are covalently cross-linked with the assistance of a crosslinker and thermal initiator, and the mixed SA molecules are uniformly dispersed in the PAM polymer network. In the second stage, the CA polymer network is formed by soaking the obtained PAM-SA hydrogel into a salt solution containing Ca^{2+}, since it can replace the Na^+ in the carboxylic acid groups of two nearby SA molecules and crosslink them with ionic bonds. As a result, PAM-CA hydrogel with a homogeneous interpenetrating 2D double network structure is successfully obtained. It can be seen from Figure S1 (Supporting Information) that the prepared PAM-CA hydrogel shows good flexibility and can be bent, twisted, and stretched at will, fully adapting to the requirements of comfortable wearing. Thanks to the greatly increased cross-linking density, the PAM-CA hydrogel shows increased mechanical strength.

To quantitatively evaluate the effect of hydrogel components on the mechanical properties, the stress-strain curves of pristine PAM, PAM-SA, and PAM-CA hydrogels are measured (Figure S2, Supporting Information). Benefiting from the numerous dynamic interactions in the synthesized PAM polymer network that can serve as energy dissipation components and the outstanding structural stability brought by its covalent cross-linking, these hydrogels all show superior stretchability and can remain intact when subjected to large tensile deformations. Compared with pristine PAM and PAM-SA hydrogels, PAM-CA hydrogel exhibits a sharp increase in mechanical strength and toughness (Figure S2, Supporting Information), attributed to the formation of a double network with an intertwined structure.[37,38] To verify the successful preparation of the double network structure, the Fourier transform-infrared (FTIR) spectrum of the PAM-CA hydrogel is obtained and compared with that of pristine PAM and PAM-SA hydrogel. As depicted in Figure S3 (Supporting Information), the peaks centered at 1119, 1647, 2931, and 3182 cm^{-1} are assigned to the —NH_2 bending vibration, the C═O stretching vibration, the C—H stretching vibration, and the N—H stretching vibrations, respectively, manifesting the presence of PAM molecular chains in all samples.[39–41] Differently, a new peak at 1031 cm^{-1} appeared in the PAM-SA and PAM-CA hydrogels, attributed to the C—O—C stretching vibration, confirming the successful incorporation of alginate.[42] After the introduction of alginate, the C═O peak undergoes a slight blue shift, which indicates the existence of interaction between the two mixed molecular chains. Furthermore, the intensity of the C═O peak in the PAM-CA hydrogel is significantly enhanced, which corresponds to the statement that Ca^{2+} enables ionic cross-linking between SA molecular chains.[43]

Considering the excellent mechanical properties of PAM-CA hydrogel, it is chosen to proof-of-concept demonstrate the feasibility of the design of our flexible NO_2 sensor, with better stability and durability compared to the pristine PAM hydrogel. In addition, PAM-CA hydrogel plays a unique positive role in enhancing the NO_2 sensing performance of the device, which will be discussed later. When different metals come into contact with PAM-CA hydrogel electrolyte, they exhibit different electrode potentials due to their distinct electronic structures and chemical reactivity. In order to enable highly sensitive NO_2 detection, we select catalytically active Ag metal as the positive electrode of the cell with a higher electrode potential, so that NO_2 will be more easily reduced on it. In addition, Zn, Fe, and Cu electrodes are all explored as negative electrodes of the cell with lower electrode potentials, and the resulting constructed devices are named as Zn/PAM-CA/Ag, Fe/PAM-CA/Ag, and Cu/PAM-CA/Ag, respectively. As shown in Figure 1c, Cu/PAM-CA/Ag exhibits the lowest open-circuit voltage of 0.11 V due to the similar electrode potential of Cu and Ag, while those of Zn/PAM-CA/Ag and Fe/PAM-CA/Ag are 0.96 and 0.51 V, respectively. Taking into account the crucial role of tiny EMFs in realizing oxygen insensitivity in our designed devices, Cu/PAM-CA/Ag is considered to be the most promising for achieving highly selective NO_2 sensing.

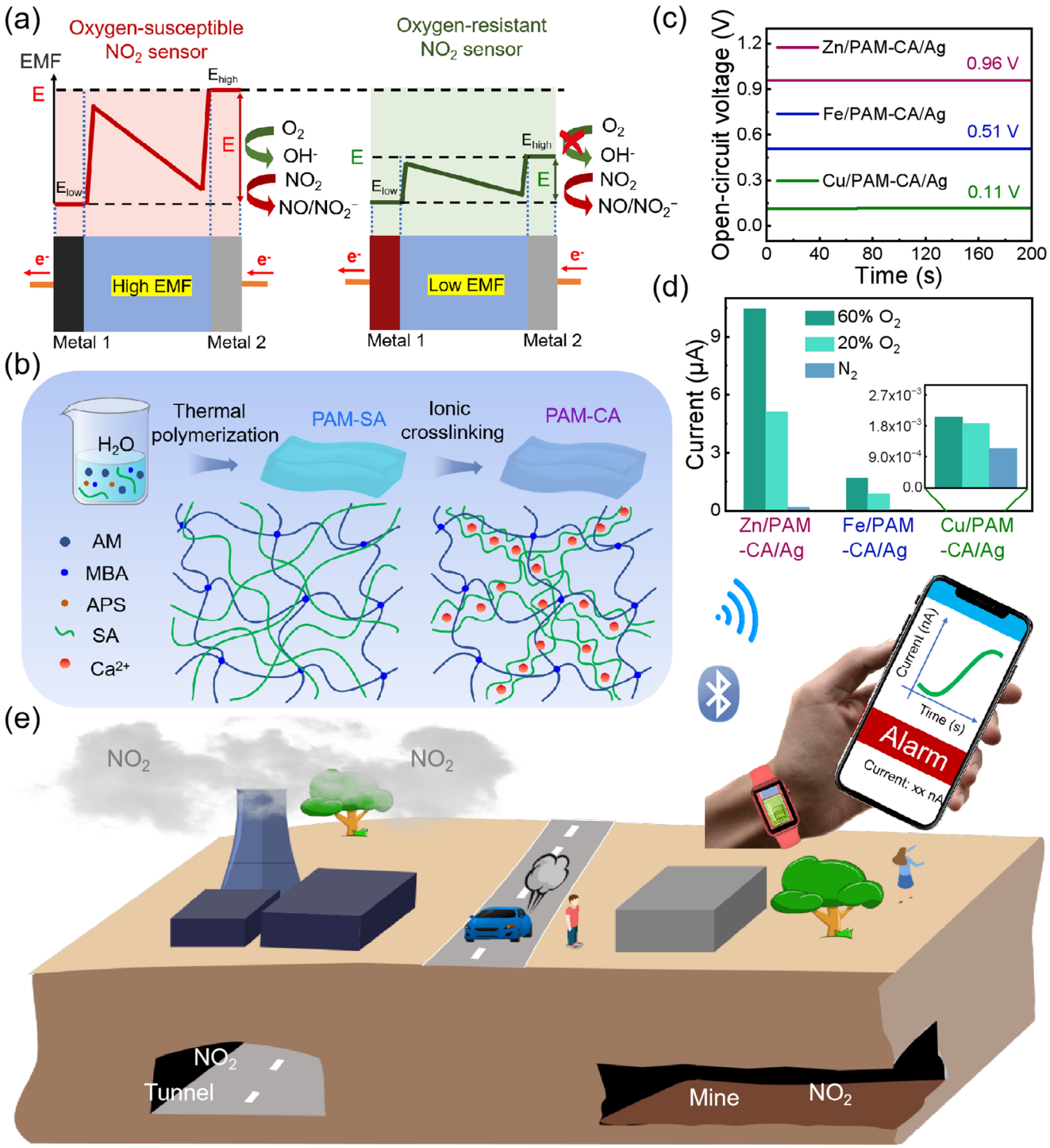

Figure 1. Design of self-powered, oxygen-resistant and flexible NO_2 sensor. a) Schematic depicting the reduction reaction of oxygen and NO_2 on electrodes with higher electrode potentials at one end of the high-EMF and low-EMF cell-structured devices, functioning as oxygen-susceptible and oxygen-resistant NO_2 sensors, respectively. b) Schematic illustration of the preparation process of PAM-CA. c) Open-circuit voltage curves of self-powered sensors with device structures of Zn/PAM-CA/Ag, Fe/PAM-CA/Ag, and Cu/PAM-CA/Ag. d) Comparison of the output currents of the three kinds of sensors in N_2, 20%, and 60% O_2. e) Schematic illustrating the application of the NO_2 sensor as a wearable device for wireless NO_2 monitoring in both atmospheric and oxygen-deficient environments.

When the two electrodes of the cell system are connected by an external circuit, the electrical current is generated spontaneously without the need for external energy. At the Cu electrode with a low electrode potential, Cu is oxidized. While at the Ag electrode with a high electrode potential, the oxidizing NO_2 undergoes a reduction reaction when exposed to NO_2. According to Faraday's law, the device current is proportional to the reactant concentration, enabling NO_2 sensing. To verify the oxygen anti-interference ability of Cu/PAM-CA/Ag, we tested its output characteristics in N_2, 20%, and 60% O_2, and compared them with those of Zn/PAM-CA/Ag and Fe/PAM-CA/Ag. As demonstrated in Figure S4 (Supporting Information) and Figure 1d, the output currents of the Cu/PAM-CA/Ag device are approximately 1.3, 1.9, and 2.1 nA in N_2, 20%, and 60% O_2, respectively, with only minor differences. In stark contrast, the output currents of Zn/PAM-CA/Ag and Fe/PAM-CA/Ag change more than 10 times when the devices are moved from N_2 to 20% and 60% O_2, indicative of much higher oxygen sensitivity, making them unsuitable for the construction of highly selective NO_2 sensors. In addition, Cu/PAM-CA/Ag has minimal current (nA level) due to the small potential difference, which is beneficial in minimizing electrode corrosion and greatly extending the service life of the sensing device. Benefiting from the self-powered, flexible, and oxygen-resistant NO_2 sensing capability of Cu/PAM-CA/Ag, it is expected to be used in combination with circuitry and wireless sensing technology as a wearable system to timely visualize NO_2 concentrations in various atmospheric environments and oxygen-deficient spaces (mines, underground tunnels, etc.), thereby ensuring the safety of the human body (Figure 1e).

2.2. Sensing Performance Characterization

Cu/PAM-CA/Ag demonstrates remarkable NO_2 sensing performance at room temperature. Upon exposure to NO_2, these target gas molecules can be adsorbed on the surface of the device and undergo electron capture and reduction reactions at the cathode–gel interface driven by the EMF, leading to an increase in the device current and the realization of the response to NO_2 (**Figure 2a**). Here, we define the device response as: $(I\text{-}I_0)/I_0$, where I_0 and I are the device currents before and after the introduction of NO_2, respectively. Figure S5 (Supporting Information) and Figure 2b show the dynamic current variation and response curves of Cu/PAM-CA/Ag to different concentrations of NO_2 from 0.1 to 2 ppm, respectively. As expected, the device current increases after being exposed to the target gas, and the current change is positively correlated with the NO_2 concentration. Upon removal of the target gas, the device current can spontaneously return to its original state driven entirely by the concentration gradient without providing additional energy, enabling reversible and repeatable sensing. As shown in Figure 2c, the device response has a good linear relationship with the NO_2 concentration ($R^2 = 0.98$). The slope of their fitting curve, that is, the device sensitivity, is evaluated to be as high as 307.17% per ppm, demonstrating that the device can accurately and efficiently detect NO_2. It is noteworthy that after exposure to NO_2, the device current first increases sharply due to the large number of electrons captured by the NO_2 reduction on the electrode. Subsequently, the device current has a significant decrease, probably due to the increase in the content of reaction products accumulated at the electrode–hydrogel interface and the corresponding decrease in the reaction rate. Finally, the device current rises again and gradually becomes stable, originating from the increase in the reduction rate of NO_2 caused by the gradual increase in the open circuit voltage after the introduction of NO_2, as shown in Figure S6 (Supporting Information).

Cu/PAM-CA/Ag shows a relatively fast response and recovery speed, enabling timely NO_2 monitoring. The response and recovery time of the sensor to 0.2 ppm NO_2, which refers to the time required for the device current to rise or fall to 90% of the final stable current after exposure or removal of the target gas, is evaluated as 41.1 and 24.6 s, respectively (Figure 2d). Even for NO_2 with the ultra-low concentration of 10 ppb, the sensor still shows obvious current response (Figure 2e). To assess the theoretical detection limit of the device, its dynamic response curve for NO_2 concentrations ranging from 30 to 150 ppb is measured (Figure S7a, Supporting Information), exhibiting a low noise level (SD = 0.41). From the response-NO_2 concentration curve, the device's sensitivity to low concentrations of NO_2 is assessed to be 0.43% per ppb (Figure S7b, Supporting Information). As a result, the theoretical detection limit of the device is calculated to be 2.86 ppb using the formula: 3SD/S, demonstrating its ability to detect trace amounts of NO_2. When the sensor is repeatedly exposed to 1 ppm NO_2, the response is highly consistent (Figure 2f), manifesting the excellent repeatability of the device. In addition, the developed devices also exhibit good consistency and reproducibility. As shown in Figure S8 (Supporting Information), three devices constructed using the same process from the same batch have similar sensitivities, which is conducive to mass production of the developed devices.

Good resistance to mechanical deformation interference is critical to the stable operation of wearable electronic devices. Thanks to the excellent mechanical flexibility of PAM-CA hydrogel, the sensor can work normally under stretching and bending deformations. As shown in Figure S9 (Supporting Information), the dynamic current variation and response curves of the sensor to 0.4–2 ppm NO_2 are compared under different mechanical deformations, including pristine, bending, and 100% strain states. It is found that no matter whether after stretching or bending, the response current and baseline current of the sensor decrease simultaneously. This is due to the fact that under mechanical deformation, the hydrogel increases in length and decreases in cross-sectional area, resulting in an increase in the internal resistance of the hydrogel due to the geometric effect as well as an increase in the charge transfer impedance at the electrode–gel interface of the device due to contact relaxation. Ultimately, the device exhibits similar sensitivity under different deformations, as demonstrated in Figure 2g, favoring its stable wearable operation.

Selectivity is a critical performance indicator of gas sensors. There are a lot of interfering gases in the atmospheric environment, including O_2, NH_3, CO_2, H_2S, and volatile organic compounds (VOCs) such as ethanol and acetone, which may have a negative impact on the NO_2 sensing performance of the device. In order to explore this, the response behaviors of Cu/PAM-CA/Ag to these gases are characterized and compared (Figure S10, Supporting Information and Figure 2h). In obvious contrast, even if the concentrations of these interfering gases are much

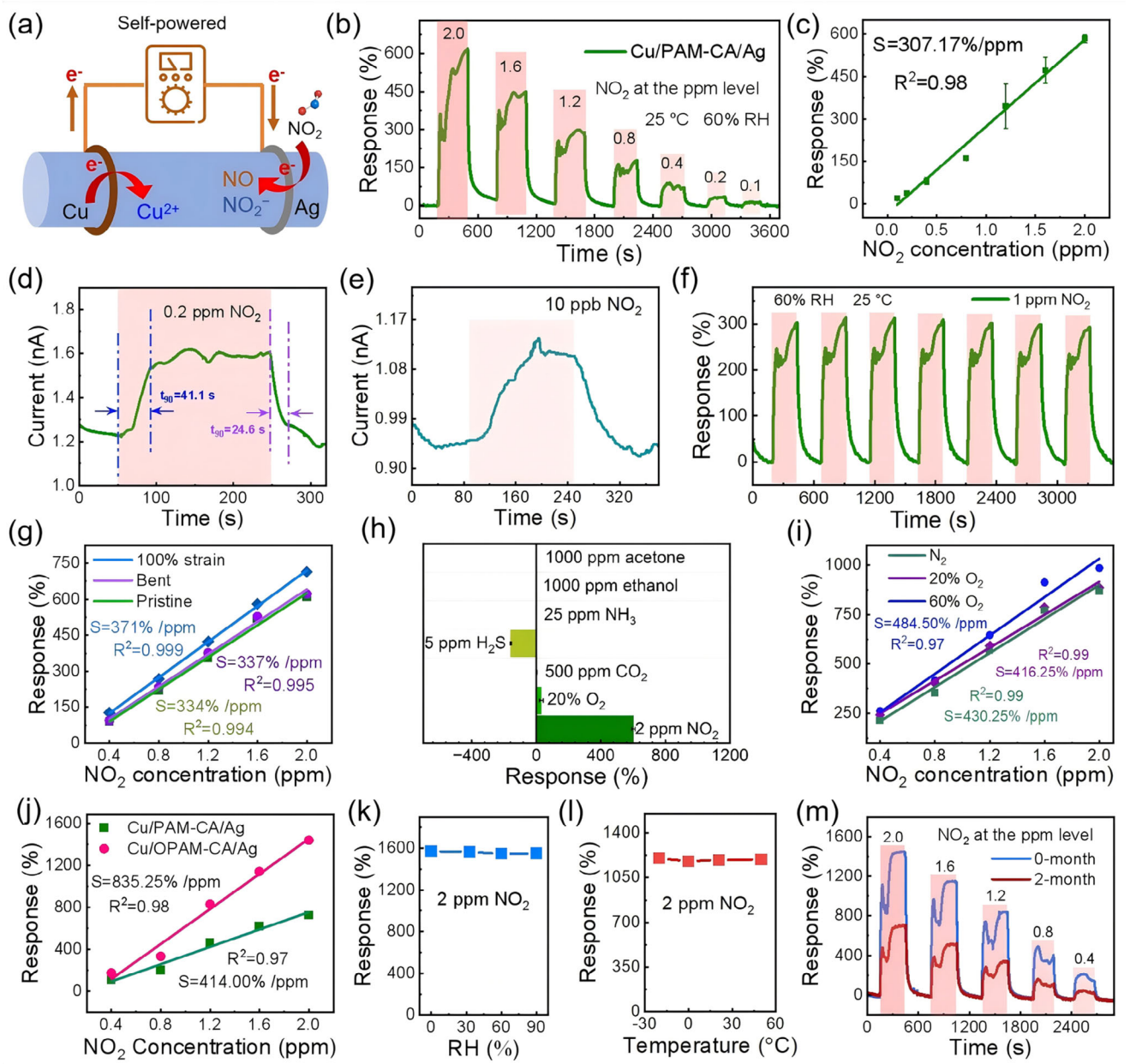

Figure 2. NO_2 sensing performance of the self-powered flexible NO_2 sensor. a) Schematic illustrating the device structure of Cu/PAM-CA/Ag. b) Dynamic response curve of Cu/PAM-CA/Ag against 0.1–2 ppm NO_2. c) Experimentally obtained and linearly fitted response versus NO_2 concentration relationship. d) Response and recovery time analysis of Cu/PAM-CA/Ag to 0.2 ppm NO_2. e) Dynamic current variation curve of Cu/PAM-CA/Ag to 10 ppb NO_2. f) Repeated response curves of the sensor to 1 ppm NO_2. g) Response-NO_2 concentration curves of Cu/PAM-CA/Ag under different mechanical deformations, including pristine, bent and 100% tensile strain. h) Comparison in responses of Cu/PAM-CA/Ag to 2 ppm NO_2 and different interfering gases including 1000 ppm acetone, 1000 ppm ethanol, 25 ppm NH_3, 5 ppm H_2S, 500 ppm CO_2, and 20% O_2. i) Response-NO_2 concentration curves of Cu/PAM-CA/Ag in N_2, 20%, and 60% O_2. j) Response-NO_2 concentration curves of Cu/PAM-CA/Ag and Cu/OPAM-CA/Ag. Response comparison of Cu/OPAM-CA/Ag to 2 ppm NO_2 at different k) humidity levels and l) temperatures. m) Dynamic response curves of Cu/OPAM-CA/Ag to 0.4–2 ppm NO_2 before and after 2-month placement of the sensor.

higher, the device's response to 2 ppm NO_2 is much higher than that to them, demonstrating the good selectivity of the device. This is attributed to the fact that in our designed system, other gases except the strongly oxidizing NO_2 are difficult to be reduced or oxidized at the electrode–gel interface driven by such a small EMF. The slight response of the device to CO_2 and NH_3 originates from their dissociation in the water-rich environment of hydrogel, which leads to an increase in ion concentration and a slight increase in device current. Differently, when exposed to H_2S, the device current decreases, which is derived from the decrease in the open circuit voltage of the device (Figure S11a, Supporting Information). This is because H_2S molecules can be

adsorbed on the Ag electrode due to the sulfur affinity of Ag metal, decreasing the electrode potential of the Ag electrode and thus the open circuit voltage of the device (Figure S11b, Supporting Information).

Among these gases, oxygen is the most interfering gas for electrochemical NO_2 sensors due to their similar oxidizing characteristics. Notably, the Cu/PAM-CA/Ag only displays a slight response to 20% O_2, ascribing to its extremely small EMF, indicating good resistance to oxygen interference. To further explore this effect, the response behavior of the device to 0.4–2 ppm NO_2 is measured under different background oxygen concentrations (Figure S12, Supporting Information). It can be found that the NO_2 sensor displays similar sensitivity with increased O_2 concentration in the background gas due to the same rising baseline current and response current (Figure 2i), allowing the device to operate normally in both oxygen-free, ambient, and oxygen-rich environments without reading variation. Compared with previously reported NO_2 sensors based on different sensing materials and device structures, the Cu/PAM-CA/Ag developed here not only exhibits superior comprehensive sensing performance at room temperature, but also features self-powering capability, resistance to oxygen interference, good flexibility and stretchability (Table S1, Supporting Information),[16,44–55] which can well meet the increasing demands of wearable electronics.

In practical applications, good environmental stability is also one of the important performance indicators. Unfortunately, hydrogels generally suffer from water loss due to the lower partial pressure of water vapor in the atmosphere after long-term exposure to air, leading to device instability and shortened service life (Figure S13, Supporting Information). To solve this, the PAM-CA organohydrogel (abbreviated as OPAM-CA) is prepared through a solvent replacement strategy, in which part of the water is replaced by glycerol, showing enhanced moisturizing properties. To verify this, we record changes in the mass of PAM-CA and OPAM-CA at different time intervals after placing them in different humidity environments (11%, 22%, and 59% RH). As shown in Figure S14 (Supporting Information), OPAM-CA always exhibits a smaller mass loss rate and mass loss. Even in a dry environment with 11% RH, the mass loss of OPAM-CA placed for 76 h was only 46.5%, which was significantly lower than that of PAM-CA (76.2%). The enhanced moisturizing properties are attributed to the formation of abundant hydrogen bonds between the hydroxyl groups of glycerol and water molecules. Notably, the assembled sensor based on Cu/OPAM-CA/Ag shows improved NO_2 sensing performance, as its sensitivity increases to as high as 835.25% per ppm, as illustrated in Figure S15 (Supporting Information) and Figure 2j. This is attributed to the significant decrease in baseline current caused by the increase in the internal resistance of the hydrogel after the introduction of organic solvent. In addition to the moisturizing effect, the freeze resistance of the hydrogel is also enhanced by the introduced glycerol, which inhibits the formation of hydrogen bonds between water molecules and the formation of ice crystals.[56] The differential scanning calorimetry (DSC) curves of PAM-CA and OPAM-CA in Figure S16 (Supporting Information) show that the freezing point of OPAM-CA drops from −18.1 to −33.6 °C, verifying the enhanced frost resistance. Thanks to these, the environmental tolerance of Cu/OPAM-CA/Ag is boosted, greatly expanding its application scenarios.

The impact of environmental (humidity and temperature) variations on the gas sensing performance is explored by comparing the response behaviors of Cu/OPAM-CA/Ag to 2 ppm NO_2 at different humidity (0, 33, 60, and 90% RH) and temperatures (−20, 0, 21, and 50 °C), manifesting that Cu/OPAM-CA/Ag can remain intact in various harsh environments. As shown in Figure S17 (Supporting Information), both the baseline current of Cu/OPAM-CA/Ag and its response current after exposure to 2 ppm NO_2 rise with increasing humidity and have similar growth trends. This is because water molecules can be adsorbed to the electrode interface to decrease the interface impedance, thereby promoting the device response process. As a result, Cu/OPAM-CA/Ag exhibits a similar response to 2 ppm NO_2 (Figure 2k), which is conducive to the stable operation of the device in different humidity environments. Similarly, Cu/OPAM-CA/Ag can operate stably in the temperature range of −20–50 °C, as both its baseline current and response current increase in the same trend with temperature due to the increase in reaction rate at high temperatures, resulting in the stable response value to 2 ppm NO_2 at different temperatures (Figure S18, Supporting Information and Figure 2l). Notably, Cu/OPAM-CA/Ag exhibits good long-term stability. Figure S19 (Supporting Information) shows the response behavior of Cu/OPAM-CA/Ag to 0.4–2 ppm NO_2 before and after 2-month placement in ambient air. Despite the decrease in NO_2 responsiveness due to the reduction in moisture content of OPAM-CA, Cu/OPAM-CA/Ag still enables the determination of NO_2 concentration (Figure 2m), showing an extended service life.

2.3. NO_2 Sensing Mechanism and Performance Optimization

Instead of changes in the electrical signal caused by the adsorption and dissociation of NO_2 molecules in the hydrogel, the response of our developed device originates from the redox reaction of the target gas molecules at the electrode–gel interface. To demonstrate this, the responses to 2 ppm NO_2 are compared for pristine, Cu electrode- and Ag electrode-covered devices, as present in **Figure 3a**. Obviously, the device response almost disappears only when the Ag electrode is covered, indicating that the response of NO_2 occurs at the Ag electrode with a higher electrode potential. Furthermore, since a mixed dilute hydrochloric acid solution of naphthylethylenediamine hydrochloride and p-aminobenzenesulfonamide can recognize NO or nitrite ions (NO_2^-) by turning its color from yellow-brown to purple-red through diazotization and coupling reactions, the color appearance of the devices consisting of the hydrogel soaked in this chromogenic agent is recorded before and after 5 min of operation in open and closed circuit modes when exposed to 5 ppm NO_2. In open circuit mode, the entire hydrogel changed from yellow-brown to faint purple-red even though no electrode reaction occurred (Figure 3b). This is attributed to the solubilization of NO_2 in water-rich conditions, with charge transfer occurring only between atoms/molecules, as illustrated in Equation 1:

$$3NO_2 + H_2O = 2HNO_3 + NO \quad (1)$$

By contrast, in closed circuit mode, the hydrogel near the Ag electrode side exhibits a deeper purple-red color compared to that

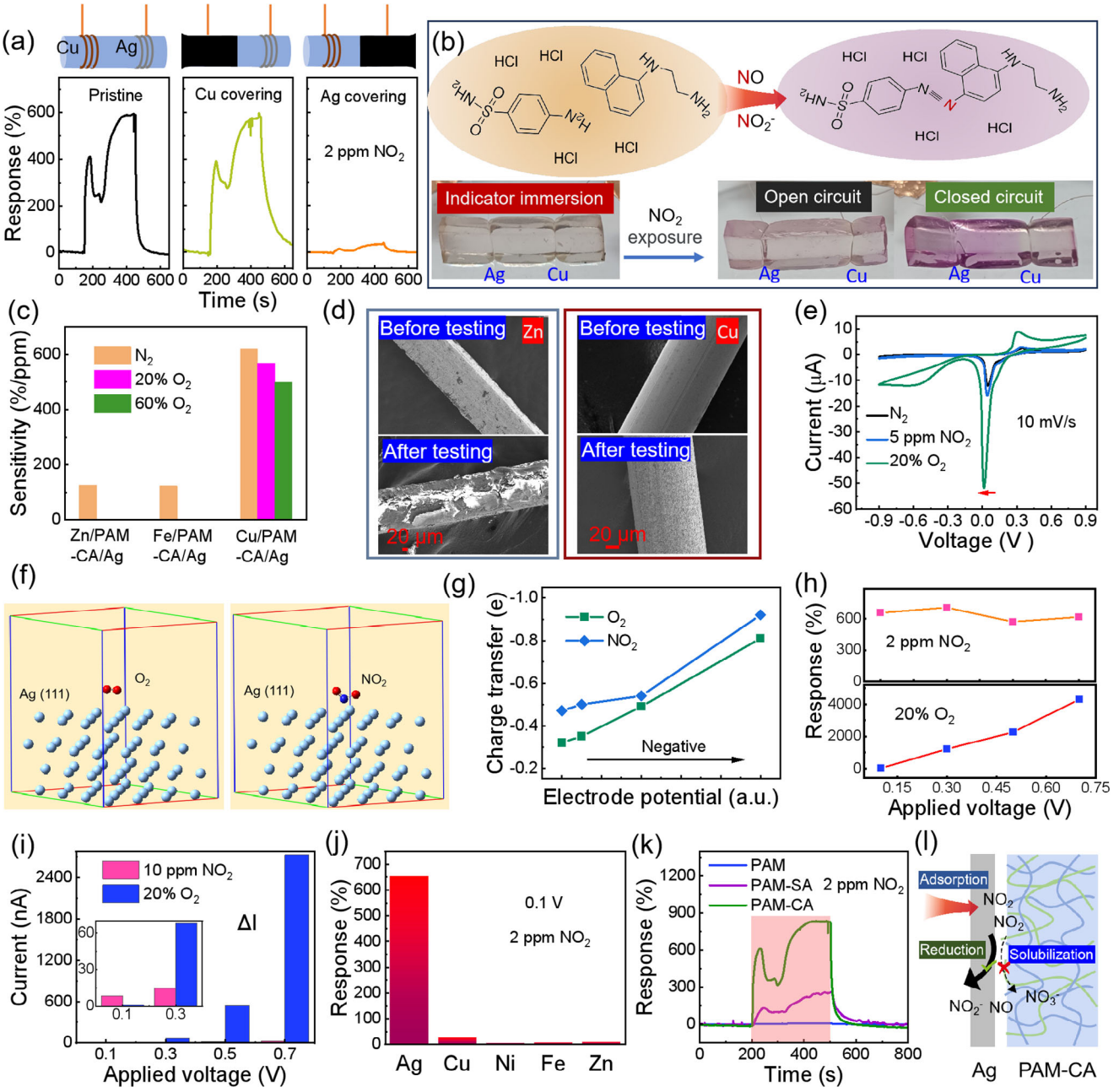

Figure 3. NO_2 sensing mechanism of the self-powered NO_2 sensor. a) Comparison in dynamic responses of pristine, Cu electrode- and Ag electrode-covered devices to 2 ppm NO_2. b) Changes in color appearance of devices assembled from PAM-CA hydrogel impregnated with a mixed dilute hydrochloric acid solution of naphthylethylenediamine hydrochloride and p-aminobenzenesulfonamide before and after 5 min of exposure to 5 ppm NO_2 running in open and closed circuit modes, respectively. c) Sensitivity comparison of Zn/PAM-CA/Ag, Fe/PAM-CA/Ag, and Cu/PAM-CA/Ag in N_2, 20%, and 60% O_2. d) SEM images of Zn and Cu electrodes in Zn/PAM-CA/Ag and Cu/PAM-CA/Ag before and after 10 h of testing in air. e) CV curves of Cu/OPAM-CA/Ag in N_2, 5 ppm NO_2, and 20% O_2. f) Adsorption structure of O_2 and NO_2 molecules on Ag (111) surface. g) Comparison of charge transfer numbers between O_2/NO_2 and Ag electrodes at different electrode potentials. Comparison of h) magnitude of response and i) response current of Ag/PAM-CA/Ag to 2 ppm NO_2 and 20% O_2 at different applied bias voltages. j) Comparison in responses of Ag/PAM-CA/Ag, Cu/PAM-CA/Cu, Ni/PAM-CA/Ni, Fe/PAM-CA/Fe, and Zn/PAM-CA/Zn to 2 ppm NO_2 when applied with a bias voltage of 0.1 V. k) Dynamic response curves of devices assembled from PAM, PAM-SA and PAM-CA to 2 ppm NO_2. l) Schematic illustrating the role of dense PAM-CA in regulating the reaction path of NO_2 at the Ag electrode–gel interface. The dissolution of NO_2 in the hydrogel is inhibited, while the reduction of NO_2 at the Ag electrode is promoted, leading to a high sensitivity.

of the Cu electrode side, further verifying the reduction of NO_2 into NO or NO_2^- at the Ag-hydrogel interface of the device by capturing electrons at the electrode, as illustrated in Equations 2 and 3:

$$NO_2 + H_2O + 2e^- \rightarrow NO + 2OH^- \quad (2)$$

$$NO_2 + e^- \rightarrow NO_2^- \quad (3)$$

The type of electrode pairs used to assemble the device is not only key to achieving immunity to oxygen interference as mentioned before, but also has an important impact on the NO_2 sensing properties of the device. As shown in Figure S20 (Supporting Information), the sensing behaviors of Fe/PAM-CA/Ag and Zn/PAM-CA/Ag to 0.4–2 ppm NO_2 are studied. It is clear that they show lower sensitivities (123.00% and 126.12% per ppm, respectively) than that of Cu/PAM-CA/Ag, attributed to their high baseline current in nitrogen driven by high EMF. In comparison, both Fe/PAM-CA/Ag and Zn/PAM-CA/Ag display ultra-high responsiveness to 20% O_2 (Figure S21, Supporting Information), as their high EMF is sufficient to drive the ORR at the Ag electrode. This is unfavorable to selective NO_2 sensing, since the NO_2 sensing abilities of Fe/PAM-CA/Ag and Zn/PAM-CA/Ag almost disappear in the environments of 20% and 60% O_2 (Figure S22, Supporting Information). In sharp contrast, Cu/PAM-CA/Ag can not only detect NO_2 more sensitively, but also has similar sensitivity when the oxygen concentration changes (Figure 3c), which is advantageous for accurate measurement of NO_2 in practical applications. In addition, due to the tiny EMF of Cu/PAM-CA/Ag, the service life of the device can be greatly prolonged. As shown in Figure 3d, when Zn/PAM-CA/Ag is operated in air for 10 h, the Zn electrode is significantly corroded due to the rapid oxidation reaction of Zn under higher EMF and the high output current, resulting in a shortening of service life. Differently, the Cu electrode in Cu/PAM-CA/Ag does not suffer from appreciable corrosion under the same circumstances, because of the slow electrode reaction rate driven by the small EMF and the slight output current, which is conducive to the continuous long-term usage of the device. For the Ag electrodes with high electrode potentials of Zn/PAM-CA/Ag and Cu/PAM-CA/Ag, there is no obvious corrosion as only the ORR occurs (Figure S23, Supporting Information).

In order to further clarify the mechanism of resistance to oxygen interference, we tested the cyclic voltammetry (CV) curves of the Cu/PAM-CA/Ag in the environment of N_2, 5 ppm NO_2, and 20% O_2 (Figures 3e and S24, Supporting Information). In N_2, the reduction peak can be attributed to the reduction of Ag^+. In 5 ppm NO_2 and 20% O_2, it can be observed that both reduction peak currents increase, which is attributed to the superposition of the reduction of NO_2 and O_2. The difference is that the reduction peak in 20% O_2 is shifted more to the left, indicating that the reduction of oxygen requires a higher EMF to drive compared to oxygen. Furthermore, the charge transfer between O_2/NO_2 molecules and Ag electrode on the surface of Ag (111) crystal face is further validated through density functional theory (DFT) calculations from an electrochemical kinetic perspective (Figure 3f). It can be found that after oxygen and NO_2 molecules adsorb on the Ag electrode, the charge transfer between gas molecules and Ag increases with the decrease of electrode potential (Figure 3g), which is consistent with the Butler-Volmer equation. More importantly, the charge transfer number between NO_2 and the Ag electrode is always higher than that between O_2 and the Ag electrode at different electrode potentials, which further demonstrates that NO_2 has a kinetically better oxidizing property than oxygen and is more easily reduced at the electrodes when applied with a tiny voltage. This provides theoretical support for the experimental results.

In order to more intuitively demonstrate the critical role of the EMF magnitude of our developed device on achieving resistance to oxygen interference, the responses of Ag/PAM-CA/Ag to 2 ppm NO_2 and 20% O_2 are compared after applying different bias voltages (0.1, 0.3, 0.5, and 0.7 V), as shown in Figures S25 and S26 (Supporting Information) and Figure 3h. Obviously, the response of Ag/PAM-CA/Ag to 2 ppm NO_2 under different bias voltages is basically consistent due to its synchronously changing baseline current and response current. By comparison, the response of Ag/PAM-CA/Ag to 20% O_2 drops from 4567.7 at a bias voltage of 0.7 V to only 17.3 at a bias voltage of 0.1 V. This is because the ORR is difficult to occur under the small bias voltage of 0.1 V, and the device only has a very small response current (Figure 3i). Therefore, the good resistance of Cu/PAM-CA/Ag to oxygen interference is proven to be attributed to its small EMF, which is not enough to drive the occurrence of ORR, providing a simple strategy to construct a highly selective NO_2 sensor.

The impact of electrode materials on the gas sensing performance is further investigated. Similar to Cu/PAM-CA/Ag, Ni/PAM-CA/Ag also has a small open circuit voltage (Figure S27a, Supporting Information). Whereas, the output current of Ni/PAM-CA/Ag cannot be maintained stable and decreases with the increase of oxygen concentration, due to the obvious decrease in the open circuit voltage of the device after the introduction of oxygen (Figure S27b—d, Supporting Information). Considering that this phenomenon does not occur in Cu/PAM-CA/Ag, we hypothesize that oxygen has a strong interaction with Ni metal and can capture its electrons for reduction, ultimately leading to a significant increase in the electrode potential of the Ni electrode. In view of this, the NO_2 sensing performance of Ni/PAM-CA/Ag in different oxygen concentration environments is also variable (Figure S28, Supporting Information), making it unsuitable for building a NO_2 sensor immune to oxygen interference here. It is found that Ag electrodes can enhance the responsiveness of the NO_2 sensor by providing a catalytic effect on the NO_2 reduction reaction. Specifically, the responses of Cu/PAM-CA/Cu, Ni/PAM-CA/Ni, Fe/PAM-CA/Fe, and Zn/PAM-CA/Zn to 2 ppm NO_2 are compared with that of Ag/PAM-CA/Ag when applied with a bias voltage of 0.1 V. It is found that the response of Ag/PAM-CA/Ag to 2 ppm NO_2 is much higher than the others, with both low baseline current and high response current (Figures 3j and S29, Supporting Information). Compared to Cu, Ni, Fe, and Zn metals, the Ag metal is the least chemically active and therefore has a high interfacial impedance when in contact with the hydrogel, resulting in a relatively low baseline current. In addition, the high response current of Ag/PAM-CA/Ag to 2 ppm NO_2 suggests the catalytic effect of the Ag metal on the reduction of NO_2 molecules adsorbed on it, thereby enabling ultrasensitive NO_2 detection.

We find that the structure and composition of the hydrogel electrolyte also affect the NO_2 sensing performance of the

assembled device. Figure S30a–c (Supporting Information) shows the dynamic current variation curves of sensors assembled from different hydrogel materials to 2 ppm NO_2, including PAM, PAM-SA, and PAM-CA hydrogels. It is obvious that the PAM-based device displays a high baseline current and a small response current when exposed to 2 ppm NO_2, resulting in an extremely low response (Figure S30d, Supporting Information and Figure 3k). Although the baseline current of the PAM-SA-based device is significantly reduced due to the decrease in conductivity and the presence of interfacial charge transfer barrier caused by the increase in polymer content, it also exhibits poor responsiveness to NO_2 due to the small response current. In comparison, the PAM-CA-based sensor not only displays low baseline current due to the double-network structure and high cross-linking density of PAM-CA hydrogels, but also exhibits high response current when exposed to 2 ppm NO_2, leading to the highest responsiveness. Since the introduction of Ca^{2+} changes both the components and the structure of PAM-SA hydrogels, we then compare the response of devices assembled from PAM hydrogel before and after soaking in 1 M $CaCl_2$ to 2 ppm NO_2 to further clarify the sensitizing effect of Ca^{2+}. Due to the absence of SA molecules, the $CaCl_2$-soaked PAM ($CaCl_2$-PAM) hydrogels do not undergo structural changes, but simply introduce a large amount of Ca^{2+} into it. As shown in Figure S31 (Supporting Information), the $CaCl_2$-PAM-based device only has a reduced baseline current compared with the pristine PAM-based one, while the response current is not significantly enhanced, indicating that Ca^{2+} cannot directly promote the reduction of NO_2.

Based on these phenomena, we can speculate that the high NO_2 responsiveness of the PAM-CA-based sensor is attributed to the unique dense double network structure of PAM-CA hydrogels. NO_2 molecules adsorbed at the electrode-hydrogel interface are mainly involved in two possible subsequent reaction paths: one is that NO_2 is reduced by acquiring electrons on the electrode, and the resulting Faradaic current significantly increases the circuit current. The other is the solubilization of NO_2 in the solvent of the hydrogel, which does not involve electron transfer on the electrodes and therefore is difficult to cause significant changes in device current. Due to the high cross-linking density in PAM-CA hydrogels, the dissolution of NO_2 in the hydrogel can be significantly inhibited, and more adsorbed NO_2 molecules can participate in the electrode reduction reaction that can cause large device current changes (Figure 3l), making PAM-CA hydrogel the most ideal candidate for building high-performance NO_2 sensors. To verify this, we compared the color appearance of PAM-SA and PAM-CA hydrogels immersed in a mixed dilute hydrochloric acid solution of naphthylethylenediamine hydrochloride and p-aminobenzenesulfonamide after exposure to the same NO_2. Obviously, the PAM-SA hydrogel exhibits stronger purple intensity (Figure S32, Supporting Information) and thus more NO_2 molecules are dissolved in it, verifying the inhibitory effect of the dense double network structure of the PAM-CA hydrogel on NO_2 solubilization. As shown in Figure S33 and S34 (Supporting Information), we measured the dynamic response curves of devices assembled from PAM-SA hydrogels soaked in $CaCl_2$ for different times (0, 1, and 3 h) and with different concentrations (0.1, 1, and 2 M) to 2 ppm NO_2. The results show that the device response to 2 ppm NO_2 increases with increasing immersion time and $CaCl_2$ concentration, attributed to the increased cross-link density of the CA network, further verifying the sensitization mechanism of PAM-CA networks.

2.4. Applications

Since our developed NO_2 sensors are self-powered, flexible, highly sensitive, and resistant to oxygen interference, they show great potential as wearable devices for timely, convenient, continuous, and accurate NO_2 detection in various scenarios. To proof-of-concept demonstrate this, a portable NO_2 sensing system is constructed by connecting the developed NO_2 sensor with a specially designed printed circuit board (PCB) consisting of signal conditioning circuit, microprocessor, Bluetooth module, and a lithium battery (**Figures** 4a and S35–S37, Supporting Information). As a result, the conditioning circuit can adjust the electrical signal collected by the NO_2 sensor, which contains information about the NO_2 concentration in the surrounding environment, to the input range of the analog-to-digital converter (ADC) in the microprocessor by means of amplification and filtering. After the microprocessor converts the processed signals into digital signals, it can be further wirelessly transmitted to a user terminal device, such as a smartphone, via a Bluetooth module. Eventually, the signals received on the smartphone can be displayed in a self-programmed App after appropriate processing and analysis, allowing the visualization of real-time sensor signals. By setting a threshold, the alarm is triggered when the collected real-time signal is higher than the threshold, and the green "NORMAL" sign displayed in the middle of the interface of the App changes to a red "ALARM" sign to remind humans of the occurrence of NO_2 leakage, thus realizing the construction of a wireless NO_2 leakage alarm system (Figure 4b).

Next, the constructed wireless NO_2 leakage alarm system is leveraged for real-time NO_2 monitoring in an anaerobic environment. The anaerobic environment is simulated by a self-made container that is dynamically supplied with dry nitrogen, and NO_2 leakage occurs after NO_2 calibration gas is also injected into it. During the test, the sensor is placed into the container and connected to the electrical circuit system. As shown in Figure 4c and Movie S1 (Supporting Information), the real-time current of the sensor is synchronously displayed on the smartphone's self-programming App interface, with a green "NORMAL" sign in the middle before NO_2 gas is passed in. As soon as 2 ppm NO_2 is introduced into the container, the collected current begins to increase. When the device signal rises above the set threshold, the green "NORMAL" sign in the middle of the APP interface turns into a red "ALARM" sign, activating the alarm function. After removing the NO_2 atmosphere, the collected sensor current begins to drop, and the alarm is lifted when it is lower than the alarm threshold. When the transmission data received on the mobile terminal is uploaded to the cloud synchronously, users in different locations can download the real-time data from the cloud using another terminal, enabling remote NO_2 detection and leak alarms (Figure S38 and Movie S2, Supporting Information). Finally, we have also demonstrated the feasibility of the designed system to realize a wireless NO_2 leakage alarm in an aerobic environment. In this case, the device is directly placed into the air. As expected, thanks to the good immunity to oxygen interference of our developed sensor, the alarm is also triggered when

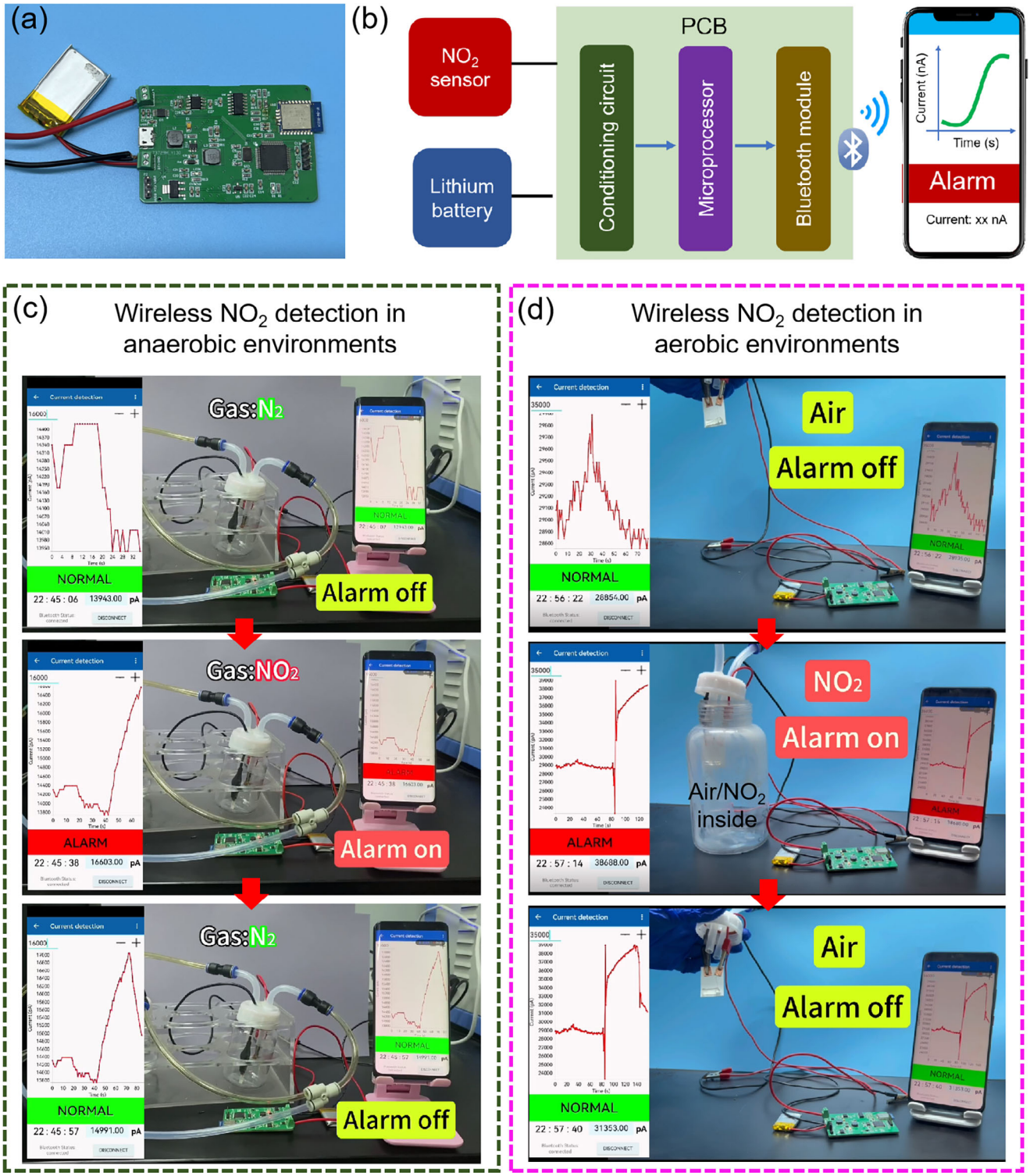

Figure 4. Wireless NO_2 monitoring with the self-powered sensor in both anaerobic and aerobic environments. a) Optical image of the self-designed PCB. b) Schematic illustrating the components of wireless NO_2 leakage alarm system, consisting of the developed NO_2 sensor, a power supply, the PCB with integrated conditioning circuits, a microprocessor, a Bluetooth module, and a smartphone as the end device. c) Real-time NO_2 monitoring in anaerobic environments: the alarm is triggered when 2 ppm NO_2/N_2 gas flows through the gas line into the test bottle for a short period of time, and then turned off when NO_2 gas is removed. d) Real-time NO_2 monitoring in aerobic environments: the alarm is triggered when the device is moved from the air to a test bottle containing trace amount of NO_2 gas for a short period of time, and then turned off when the device is moved to the air again.

the device is moved from the air into a plastic bottle containing traces of NO_2 gas balanced with air for a short period of time, as demonstrated in Figure 4d and Movie S3 (Supporting Information). Given these results, the timely, accurate, and efficient identifications of NO_2 leakage with the sensor in both aerobic and anaerobic environments are demonstrated, which can avoid the huge risks caused by this toxic gas leakage event, showing great application potential in practice.

3. Conclusion

In summary, we have developed a novel self-powered, stretchable, and oxygen-resistant/independent NO_2 sensor with a cell structure, consisting of a tough PAM-CA hydrogel and a specific heterogeneous metal electrode pair with a tiny electrode potential difference for regulating the redox reaction occurred at the electrodes. The sensor not only exhibits outstanding NO_2 sensing performance, including high sensitivity (307.17% per ppm), good repeatability, remarkable selectivity, and ultra-low LOD (2.84 ppb), but also gains desirable resistance to oxygen and mechanical deformation interferences. The high responsiveness is attributed to the catalytic effect of the Ag electrode on the reduction reaction of NO_2 and the hindering effect of the high-density double-networked PAM-CA hydrogel on the NO_2 solubilization process, allowing the adsorbed NO_2 molecules on the hydrogel–electrode interface to effectively participate in the electrode reduction reaction that can cause large device current changes. Through rational experimental analysis and theoretical calculations, the oxygen insensitivity of the device arises from the kinetically higher oxidizing activity of NO_2 compared to oxygen, and the small potential difference provided by the device struggles to drive the ORR to occur, providing a facile strategy to design highly selective NO_2 sensors. By introducing glycerol into the PAM-CA hydrogel, the environmental tolerance and service life of the sensor are greatly improved, enabling it to operate normally under various harsh conditions (dry, humid, low, and high temperature environments) with unimpaired performance. As a proof-of-concept demonstration, a wireless NO_2 leak alarm system is designed by combining our developed NO_2 sensor with wireless communication technology. Regardless of whether it is in an aerobic or anaerobic environment, the system can promptly alarm when NO_2 gas is leaked, which verifies its broad application prospects in various scenarios. This work may inspire the design of more selective and sensitive electrochemical gas sensors by modulating the hydrogel electrolytes and electrodes for regulating the reaction paths of analytes. Since water loss in hydrogels is still unavoidable even after the introduction of organic solvents, the stability of the developed devices is limited, which needs to be vigorously addressed in the future by selecting non-aqueous flexible gel materials or gas-permeable encapsulation film.[57]

4. Experimental Section

Preparation of PAM, PAM-SA, and PAM-CA Hydrogels: The synthesis of PAM and PAM-SA hydrogels was implemented through a straightforward one-pot thermal polymerization strategy. For PAM hydrogels, first, 9.333 g of AM was added to 60 mL of deionized water (DI) with continuous stirring at 600 rpm until the polymer monomer was completely dissolved. Then, 4 mg of N, N"-Methylene bisacrylamide (MBA), 30 µL of N, N, N", N'-tetramethylethylenediamine, and 56.1 mg of ammonium persulphate (APS) were sequentially added to the precursor solution of the hydrogel, functioning as a cross-linking agent, accelerator, and thermal initiator, respectively. Finally, the resulting transparent solution was placed in a plastic petri dish and left in an oven at 65 °C for 2 h. After cooling to room temperature, the PAM hydrogel was formed. The specific steps for preparing PAM-SA hydrogels were the same as those for PAM hydrogels, except that 9.333 g of AM and 1.167 g of SA needed to be dissolved together in 60 mL DI in the first step. PAM-CA hydrogels were obtained by immersing the prepared PAM-SA hydrogels in 1 M $CaCl_2$ solution for 3 h.

Materials Characterization: The stress–strain curves of hydrogels were obtained from a tensile testing machine (Wavetest, Instron 5943). The FTIR spectra of hydrogels were acquired by Fourier transform infrared spectroscopy-microscope (Thermo Fisher, NICOLET 6700), with the wavenumber range of 600–4000 cm^{-1}. The DSC curves of hydrogels were characterized by a differential scanning calorimeter (Netzsch, DSC-204), in which the samples were cooled at a rate of 5 °C min^{-1} from 15 to −120 °C with nitrogen flow. The SEM images of the electrodes before and after device operation were acquired using a field emission scanning electron microscope (Wavetest, SUPRA 60). The CV curves of the devices under different atmospheres were recorded by an electrochemical workstation (CH Instruments, CHI760E).

Device Fabrication: The prepared PAM-CA hydrogel was first cut into small pieces measuring 150 × 30 × 30 mm to serve as a solid electrolyte. Subsequently, Cu and Ag metal wires were wound around both ends of the hydrogel as electrodes, with diameters of 100 and 60 µm, respectively. The distance between the two metal electrodes was set at 40 mm during all the sensing tests. The constructed device was stored in a refrigerator at 0 °C and sealed when not in use.

Gas Sensing Characterization: The gas sensing performance of sensors was characterized in a homemade dynamic gas dilution and distribution system, consisting mainly of a DGL-III gas and liquid distribution instrument, a digital mass flow controller (MFC), and a plastic gas washing cylinder as a gas chamber. During the test, the current of the sensor placed in the gas chamber was recorded by an electrochemical workstation (CH Instruments, CHI760E) without the need to apply additional bias voltage. The background gas, NO_2 standard gas, and moist nitrogen gas produced by the bubbling method were mixed at different flow rates to obtain NO_2 gas with a specific concentration and humidity level, and their total flow rate needed to be kept constant. The NO_2 sensing performance of the device in an anaerobic environment was tested by using nitrogen as the background gas, while that of the device in an aerobic environment was measured by using oxygen as the background gas, where the oxygen concentration was regulated by varying its flow rate. The selectivity of the device was tested by passing other types of standard gas or nitrogen mixed with organic gases, instead of the NO_2 standard gas, into the test vessel. Gas testing at 50 °C was carried out by placing the test vessel and part of the gas flow tubes in a constant-temperature oil bath, so that the gas can be heated to the set temperature. Gas testing at 0 and −20 °C was carried out by placing the test vessel and part of the gas flow tubes in a low-temperature cooling liquid circulation pump. Unless otherwise specified, the gas sensing tests were performed at 25 °C and 60% RH.

DFT Calculation: The DFT calculations were performed to study the O_2 and NO_2 adsorption mechanism for the Ag slab. The Perdew-Burke-Ernzerhof (PBE) functional within the generalized gradient approximation (GGA) method and Broyden–Fletcher–Goldfarb–Shanno update scheme was utilized.[58,59] The ultrasoft pseudopotential formalism was applied in our simulation system, and the energy cutoff of electron wave function was set as 300 eV.[60] The O_2 and NO_2 molecules were put in the vicinity on the Ag slab (1 1 1) substrates in the simulation box with dimensions of about 10.0 × 11.6 × 17.1 $Å^3$, respectively. The O_2 and NO_2 were adsorbed on the Ag slab after the geometry optimization by the freezing position of the Ag slab with 0 1 4 10 e to mimic the different applied potential in the experiment. And then, the adsorption energy and the transferred charge of O_2 and NO_2 molecules were obtained by the energy difference during the adsorption process.

Statistical Analysis: Data are shown as the mean ± standard deviation (SD). The error bars in the various data graphs represent SDs for at least two tests on each sample, which represent SDs for test on two samples. All data were processed using Origin 2024b.

Supporting Information

Supporting Information is available from the Wiley Online Library or from the author.

Acknowledgements

Q.D., Y.L., W.S., H.W., J.L., and Y.Z. contributed equally to this work. The authors acknowledge financial supports from the National Natural Science Foundation of China (22475243, 62401403, 61801525), the National Key Research and Development Program of China (2024YFA1207804), and the Foundation of the state key Laboratory of Transducer Technology (No. SKT2301).

Conflict of Interest

The authors declare no conflict of interest.

Data Availability Statement

The data that support the findings of this study are available in the Supporting Information of this article.

Keywords

dense hydrogel network, flexible gas sensors, flexible hydrogel sensors, oxygen-resistant NO_2 sensors, self-powered sensor

Received: May 21, 2025
Revised: June 28, 2025
Published online: July 18, 2025

[1] B. Wang, A. Thukral, Z. Xie, L. Liu, X. Zhang, W. Huang, X. Yu, C. Yu, T. J. Marks, A. Facchetti, *Nat. Commun.* **2020**, *11*, 2405.
[2] W. Huang, Q. Ding, H. Wang, Z. Wu, Y. Luo, W. Shi, L. Yang, Y. Liang, C. Liu, J. Wu, *Nat. Commun.* **2023**, *14*, 5221.
[3] J. Shin, K. Kim, I. S. Min, M. Sang, J. Y. Lee, K. Hwang, Y. Kang, J. Kim, K. J. Yu, *Adv. Funct. Mater.* **2024**, *35*, 2419110.
[4] J. Li, H. Wang, Y. Luo, Z. Zhou, H. Zhang, H. Chen, K. Tao, C. Liu, L. Zeng, F. Huo, J. Wu, *Nano-Micro Lett.* **2024**, *16*, 256.
[5] R. D. Brook, S. Rajagopalan, C. A. Pope III, J. R. Brook, A. Bhatnagar, A. V. Diez-Roux, F. Holguin, Y. Hong, R. V. Luepker, M. A. Mittleman, A. Peters, D. Siscovick, S. C. Smith, L. Whitsel, J. D. Kaufman, *Circulation* **2010**, *121*, 2331.
[6] W. Huang, X. Zhuang, F. S. Melkonyan, B. Wang, L. Zeng, G. Wang, S. Han, M. J. Bedzyk, J. Yu, T. J. Marks, A. Facchetti, *Adv. Mater.* **2017**, *29*, 1701706.
[7] J. Zhang, X. Liu, G. Neri, N. Pinna, *Adv. Mater.* **2016**, *28*, 795.
[8] G. Jiang, M. Goledzinowski, F. J. Comeau, H. Zarrin, G. Lui, J. Lenos, A. Veileux, G. Liu, J. Zhang, S. Hemmati, J. Qiao, Z. Chen, *Adv. Funct. Mater.* **2016**, *26*, 1729.
[9] Z. Wu, H. Wang, Q. Ding, K. Tao, W. Shi, C. Liu, J. Chen, J. Wu, *Adv. Funct. Mater.* **2023**, *33*, 2300046.
[10] G. Korotcenkov, S. D. Han, J. R. Stetter, *Chem. Rev.* **2009**, *109*, 1402.
[11] C. Yang, Z. Suo, *Nat. Rev. Mater.* **2018**, *3*, 125.
[12] L. Hu, P. L. Chee, S. Sugiarto, Y. Yu, C. Shi, R. Yan, Z. Yao, X. Shi, J. Zhi, D. Kai, H. Yu, W. Huang, *Adv. Mater.* **2023**, *35*, 2205326.
[13] X. Li, J. P. Gong, *Nat. Rev. Mater.* **2024**, *9*, 380.
[14] K. Tao, J. Yu, J. Zhang, A. Bao, H. Hu, T. Ye, Q. Ding, Y. Wang, H. Lin, J. Wu, H. Chang, H. Zhang, W. Yuan, *ACS Nano* **2023**, *17*, 16160.
[15] Y. Luo, H. Wang, Y. Liang, R. Xie, Z. Wu, Y. Zhou, K. Tao, S. Pan, B. R. Yang, Y. Fu, F. Liu, F. Huo, J. Wu, *Adv. Funct. Mater.* **2025**, 2502196.
[16] Z. Wu, L. Rong, J. Yang, Y. Wei, K. Tao, Y. Zhou, B. R. Yang, X. Xie, J. Wu, *Small* **2021**, *17*, 2104997.
[17] L.-Y. Zhu, L.-X. Ou, L.-W. Mao, X.-Y. Wu, Y.-P. Liu, H.-L. Lu, *Nano-Micro Lett.* **2023**, *15*, 89.
[18] Y. K. Jo, S.-Y. Jeong, Y. K. Moon, Y.-M. Jo, J.-W. Yoon, J.-H. Lee, *Nat. Commun.* **2021**, *12*, 4955.
[19] L. Kong, C. Tang, H. J. Peng, J. Q. Huang, Q. Zhang, *SmartMat* **2020**, *1*, 1007.
[20] F. Xiang, F. Cheng, Y. Sun, X. Yang, W. Lu, R. Amal, L. Dai, *Nano Res.* **2023**, *16*, 4821.
[21] H. Dong, J. Li, J. Guo, F. Lai, F. Zhao, Y. Jiao, D. J. Brett, T. Liu, G. He, I. P. Parkin, *Adv. Mater.* **2021**, *33*, 2007548.
[22] R. Liu, Z. L. Wang, K. Fukuda, T. Someya, *Nat. Rev. Mater.* **2022**, *7*, 870.
[23] M. Gao, P. Wang, L. Jiang, B. Wang, Y. Yao, S. Liu, D. Chu, W. Cheng, Y. Lu, *Energy Environ. Sci.* **2021**, *14*, 2114.
[24] Y. H. Zhou, X. Xiao, G. R. Chen, X. Zhao, J. Chen, *Joule* **2022**, *6*, 1381.
[25] K. Tao, H. Yi, Y. Yang, H. Chang, J. Wu, L. Tang, Z. Yang, N. Wang, L. Hu, Y. Fu, J. Miao, W. Yuan, *Nano Energy* **2020**, *67*, 104197.
[26] Q. Zhou, J. Pan, S. Deng, F. Xia, T. Kim, *Adv. Mater.* **2021**, *33*, 2008276.
[27] Z. L. Wang, *Adv. Energy Mater.* **2020**, *10*, 2000137.
[28] Y. Wang, W. Zhu, Y. Deng, B. Fu, P. Zhu, Y. Yu, J. Li, J. Guo, *Nano Energy* **2020**, *73*, 104773.
[29] H. Ryu, H. J. Yoon, S. W. Kim, *Adv. Mater.* **2019**, *31*, 1802898.
[30] K. W. Sou, Z. Lin, Y. Jin, S. Ping, W. Ding, J. Wang, *Nano Energy* **2024**, *127*, 109746.
[31] G. Xiao, J. Ju, H. Lu, X. Shi, X. Wang, W. Wang, Q. Xia, G. Zhou, W. Sun, C. M. Li, Y. Qiao, Z. Lu, *Adv. Sci.* **2022**, *9*, 2103822.
[32] N. T. Garland, R. Kaveti, A. J. Bandodkar, *Adv. Mater.* **2023**, *35*, 2303197.
[33] A. Bueno-López, *Appl. Catal., B* **2014**, *146*, 1.
[34] G. Li, C. Li, G. Li, D. Yu, Z. Song, H. Wang, X. Liu, H. Liu, W. Liu, *Small* **2022**, *18*, 2101518.
[35] Q. Chen, L. Zhu, C. Zhao, Q. Wang, J. Zheng, *Adv. Mater.* **2013**, *25*, 4171.
[36] D. Yao, W. Wang, H. Wang, Y. Luo, H. Ding, Y. Gu, H. Wu, K. Tao, B. R. Yang, S. Pan, J. Fu, F. Huo, J. Wu, *Adv. Funct. Mater.* **2025**, *35*, 2416482.
[37] G. Ge, Y. Zhang, J. Shao, W. Wang, W. Si, W. Huang, X. Dong, *Adv. Funct. Mater.* **2018**, *28*, 1802576.
[38] J.-Y. Sun, X. Zhao, W. R. Illeperuma, O. Chaudhuri, K. H. Oh, D. J. Mooney, J. J. Vlassak, Z. Suo, *Nature* **2012**, *489*, 133.
[39] C. Chen, Y. Wang, Q. Wu, Z. Wan, D. Li, Y. Jin, *Chem. Eng. J.* **2020**, *400*, 125876.
[40] R. Liu, S. Liang, X.-Z. Tang, D. Yan, X. Li, Z.-Z. Yu, *J. Mater. Chem.* **2012**, *22*, 14160.
[41] Q. Ding, H. Wang, Y. Zhou, Z. Zhang, Y. Luo, Z. Wu, L. Yang, R. Xie, B. R. Yang, K. Tao, S. Pan, F. Liu, J. Fu, F. Huo, J. Wu, *Adv. Mater.* **2025**, *37*, 2502369.
[42] E. Henao, E. Delgado, H. Contreras, G. Quintana, *Int. J. Chem. Eng.* **2018**, *2018*, 3137167.
[43] Z.-K. Liu, S.-S. Deng, Y. Zhou, Z. Tong, J.-K. Liu, Z. Wang, M.-J. Guo, L. Deng, Y. Zhen, J.-T. Li, J.-M. Xu, S.-G. Sun, *ACS Appl. Mater. Interfaces* **2023**, *15*, 24416.

[44] H. Min, O. Kwon, J. Lee, E. Choi, J. Kim, N. Lee, K. Eum, K. H. Lee, D. W. Kim, W. Lee, *Adv. Mater.* **2024**, *36*, 2309041.
[45] S. Kim, J. Han, J. M. Choi, J. S. Nam, I. H. Lee, Y. Lee, I. V. Novikov, E. I. Kauppinen, K. Lee, I. Jeon, *Adv. Mater.* **2024**, *36*, 2313830.
[46] X. Geng, S. Li, L. Mawella-Vithanage, T. Ma, M. Kilani, B. Wang, L. Ma, C. C. Hewa-Rahinduwage, A. Shafikova, E. Nikolla, G. Mao, S. L. Brock, L. Zhang, L. Luo, *Nat. Commun.* **2021**, *12*, 4895.
[47] C. Park, H. Shin, M. Jeon, S.-H. Cho, J. Kim, I.-D. Kim, *ACS Nano* **2024**, *18*, 26066.
[48] J.-O. Kim, W.-T. Koo, H. Kim, C. Park, T. Lee, C. A. Hutomo, S. Q. Choi, D. S. Kim, I.-D. Kim, S. Park, *Nat. Commun.* **2021**, *12*, 4294.
[49] Z. Yang, S. Lv, Y. Zhang, J. Wang, L. Jiang, X. Jia, C. Wang, X. Yan, P. Sun, Y. Duan, F. Liu, G. Lu, *Nano-Micro Lett.* **2022**, *14*, 56.
[50] Y. Su, J. Wang, B. Wang, T. Yang, B. Yang, G. Xie, Y. Zhou, S. Zhang, H. Tai, Z. Cai, G. Chen, Y. Jiang, L.-Q. Chen, J. Chen, *ACS Nano* **2020**, *14*, 6067.
[51] T. Pham, G. Li, E. Bekyarova, M. E. Itkis, A. Mulchandani, *ACS Nano* **2019**, *13*, 3196.
[52] Y. Su, G. Xie, H. Tai, S. Li, B. Yang, S. Wang, Q. Zhang, H. Du, H. Zhang, X. Du, Y. Jiang, *Nano Energy* **2018**, *47*, 316.
[53] S. Wei, Z. Li, K. Murugappan, Z. Li, F. Zhang, A. G. Saraswathyvilasam, M. Lysevych, H. H. Tan, C. Jagadish, A. Tricoli, L. Fu, *Adv. Mater.* **2023**, *35*, 2207199.
[54] B. Liu, X. Liu, Z. Yuan, Y. Jiang, Y. Su, J. Ma, H. Tai, *Sens. Actuators, B* **2019**, *295*, 86.
[55] M. L. Jin, S. Park, H. Kweon, H. J. Koh, M. Gao, C. Tang, S. Y. Cho, Y. Kim, S. Zhang, X. Li, K. Shin, A. Fu, H.-T. Jung, C. W. Ahn, D. H. Kim, *Adv. Mater.* **2021**, *33*, 2007605.
[56] Q. Ding, Z. Wu, K. Tao, Y. Wei, W. Wang, B.-R. Yang, X. Xie, J. Wu, *Mater. Horiz.* **2022**, *9*, 1356.
[57] Z. Zhang, J. Li, H. Chen, H. Wang, Y. Luo, R. Si, R. Xie, K. Tao, B. R. Yang, D. Zhang, F. Liu, F. Huo, J. Wu, *Adv. Funct. Mater.* **2025**, 2502583.
[58] J. P. Perdew, A. Ruzsinszky, G. I. Csonka, O. A. Vydrov, G. E. Scuseria, L. A. Constantin, X. Zhou, K. Burke, *Phys. Rev. Lett.* **2008**, *100*, 136406.
[59] J. D. Head, M. C. Zerner, *Chem. Phys. Lett.* **1985**, *122*, 264.
[60] D. Vanderbilt, *Phys. Rev. B* **1990**, *41*, 7892.